Title
In situ interface engineering for probing the limit of quantum dot photovoltaic devices.

Journal
Nature nanotechnology, 14(10)

ISSN
1748-3387

Authors
Dong, Hui
Xu, Feng
Sun, Ziqi
et al.

Publication Date
2019-10-01

DOI
10.1038/s41565-019-0526-7

Peer reviewed

LETTERS
https://doi.org/10.1038/s41565-019-0526-7
nature nanotechnology

In situ interface engineering for probing the limit of quantum dot photovoltaic devices

Hui Dong[1,8,9], Feng Xu[1,9], Ziqi Sun[2,9], Xing Wu[3], Qiubo Zhang[1], Yusheng Zhai[4], Xiao Dong Tan[1], Longbing He[1], Tao Xu[1], Ze Zhang[5]*, Xiangfeng Duan[6]* and Litao Sun[1,4,7]*

Quantum dot (QD) photovoltaic devices are attractive for their low-cost synthesis, tunable band gap and potentially high power conversion efficiency (PCE). However, the experimentally achieved efficiency to date remains far from ideal. Here, we report an in-situ fabrication and investigation of single TiO_2-nanowire/CdSe-QD heterojunction solar cell (QDHSC) using a custom-designed photoelectric transmission electron microscope (TEM) holder. A mobile counter electrode is used to precisely tune the interface area for in situ photoelectrical measurements, which reveals a strong interface area dependent PCE. Theoretical simulations show that the simplified single nanowire solar cell structure can minimize the interface area and associated charge scattering to enable an efficient charge collection. Additionally, the optical antenna effect of nanowire-based QDHSCs can further enhance the absorption and boost the PCE. This study establishes a robust 'nanolab' platform in a TEM for in situ photoelectrical studies and provides valuable insight into the interfacial effects in nanoscale solar cells.

QDHSCs have attracted considerable attention for several significant merits, such as a tunable bandgap[1], high extinction coefficient[2], multiple exciton generation effect[3] and high stability against oxidative deterioration[4]. A typical QDHSC consists of a large surface area nanostructured photoanode to effectively adsorb QDs for an efficient light harvest. The photoanode also facilitates the fast collection of electrons from the QDs and transports them to a collecting electrode. The theoretical PCE of a QDHSC can reach up to 33 or 44%, depending on whether or not multiple exciton generation of the QDs is taken into consideration[5], which matches or exceeds the Shockley–Queisser limit of 33% (ref. [6]) for typical semiconductor solar cells. Despite these exciting promises, the highest certified PCE of a QDHSC reported to date is only 11.6% (ref. [7]), largely due to non-ideal interfaces that induce undesired carrier recombination and retard the charge collection efficiency.

Mesoporous nanoparticle films of TiO_2 are popular photoanodes for QDHSCs because of their appropriate band structure with respect to the QDs, as well as the possibility to effectively separate photogenerated carriers[8–10]. The conversion efficiency of a TiO_2 nanoparticle photoanode, however, is usually limited in the range of 1–3% (refs. [11–13]). This is mainly due to the presence of numerous grain boundaries and interfacial defects that act as trap centres for photogenerated carriers and increase carrier recombination. One-dimensional (1D) nanostructures are considered advantageous over nanoparticles in photoanodes because, in such structures, electron transport and collection are faster due to the availability of a direct pathway[14,15]. The practical application of 1D nanowires in QDHSCs, unfortunately, has not delivered its full promise, largely limited by the reduced surface area and active sites for the adsorption of QDs[16,17]. In another study, a significant increase in PCE up to 5.24% was achieved by taking advantage of the high surface area of 3D nanostructures, double-layer structures and branched structures[18]. Nevertheless, a number of surface and interfacial sites, which act as charge recombination centres to trap free electrons, still plague the resulting devices. To this end, a ZnS/SiO_2 double-layer coating was used to inhibit interfacial recombination, which resulted in a higher efficiency of 8.2% (ref. [19]).

Although materials innovation, bandgap engineering and heterostructure design have increased the conversion efficiency of QDHSCs from <1% in the initial works to ~11–12%, this value still falls far from the theoretical efficiency limit of 33%. Further enhancement of the PCE of QDHSC is seriously limited by the intrinsic electron loss at the interface. To push the limit of the PCE up to the theoretical value, a fundamental understanding of the physics of nanoscale heterojunctions is necessary. In this context, the development of in situ TEM techniques enables the fabrication of in situ constructed devices in a 'nanolab' inside a TEM[20]. The state-of-the-art microscopic techniques have the unique capability to study the underlying mechanism of energy devices during operation and are employed to elucidate the charge transfer and microstructure evolution during the operation of lithium-ion batteries[21] and resistive memories[22]. In these experiments, the nanolab consists of a high-performance TEM scanning tunnelling microscopy (STM) sample holder, which allows the direct visualization of the operation of nanoscale devices mounted on it. In situ studies of these energy devices can offer valuable insight for a fundamental understanding of the critical factors for further enhancing the device performance. Miller and Crozier first initiated a system inside a TEM to study in situ photocatalysts under the illumination of visible and ultraviolet lights[23]. Cavalca et al.[24] directly visualized the light-induced reduction of cuprous oxide in an environmental TEM. However, the

[1]SEU-FEI Nano-Pico Center, Key Laboratory of MEMS of Ministry of Education, Collaborative Innovation Center for Micro/Nano Fabrication, Device and System, Southeast University, Nanjing, China. [2]School of Chemistry, Physics and Mechanical Engineering, Queensland University of Technology, Gardens Point, Brisbane, Queensland, Australia. [3]Department of Electrical Engineering, East China Normal University, Shanghai, China. [4]Joint International Research Laboratory of Information Display and Visualization, School of Electronic Science and Engineering, Southeast University, Nanjing, China. [5]Department of Materials Science and Engineering, State Key Laboratory of Silicon Materials, Zhejiang University, Hangzhou, China. [6]Department of Chemistry and Biochemistry, California NanoSystems Institute, University of California, Los Angeles, CA, USA. [7]Southeast University–Monash University Joint Research Institute, Suzhou, China. [8]Present address: Key Laboratory of Welding Robot and Application Technology of Hunan Province, Engineering Research Center of Complex Tracks Processing Technology and Equipment of Ministry of Education, Xiangtan University, Xiangtan, China. [9]These authors contributed equally: Hui Dong, Feng Xu, Ziqi Sun. *e-mail: zezhang@zju.edu.cn; xduan@chem.ucla.edu; slt@seu.edu.cn

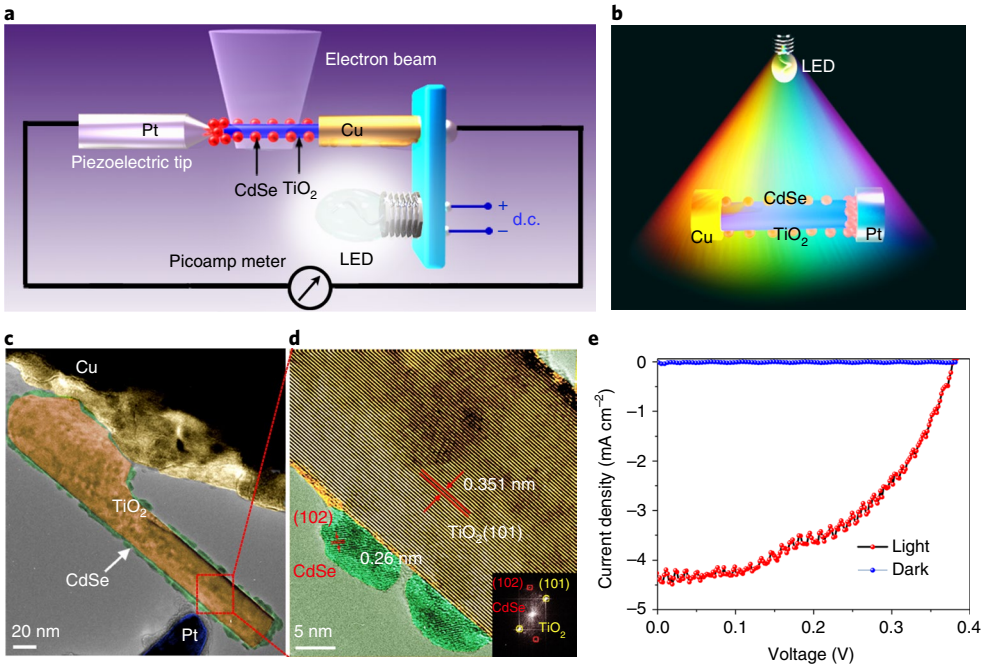

Fig. 1 | Configuration and performance of a single nanowire QDHSC. a, Schematic diagram of the in situ fabrication of an individual TiO_2/CdSe nanowire QD solar cell based on a heterojunction. The LED driven by d.c. power is placed on a sapphire substrate, which is inserted into the slot previously occupied by the electrical measurement system in the STM-TEM. A Keithley 6430 picoamp meter was used to collect the photocurrent after excitation by photoirradiation from the LED. The schematic illustration of the photoelectric nanolab designed based on a nanofactory TEM-STM holder is shown in Supplementary Fig. 2a. The details on how to install and activate the LED in a nanolab are given in Supplementary Part 2 and Supplementary Fig. 2b. This design integrates the solar cell assembly and the photoelectric measurement equipment. A shield box that consists of both d.c. and electrostatic shields was connected to the measurement system to reduce noise in the photocurrent detection. The details of the circuit diagram of the shield are given in Supplementary Fig. 3. **b**, Schematic diagram of the QDHSC exposed to white light from the LED. **c**,**d**, A low magnification TEM image of the TiO_2 nanowire with CdSe QDs (**c**) and the corresponding HRTEM images (**d**). The colours represent different parts of the constructed nanowire solar cell. **e**, A typical *J*–*V* curve of the nanowire solar cell under irradiation and the corresponding photovoltaic properties. The effect of the electron beam on the current measurement is summarized in Supplementary Fig. 5. The contribution of the electron beam to the photocurrent measurement can be properly excluded by conducting the current measurements with and without the electron beam (Supplementary Fig. 6) and therefore *J*–*V* measurements were carried out with the electron beam blanked.

complexity in designing a suitable in situ photoelectric TEM stage means that it is difficult to study the in situ assembly and observation of photoelectric devices in operation.

Here, we report the design of a state-of-the-art TEM holder by incorporating a light source within the holder without affecting the quality of high-resolution TEM (HRTEM) imaging. Using this TEM sample holder, we built a single nanowire QDHSC, with the simplest cell structure and a minimum number of interfaces. This QDHSC design offers a valuable model system to tailor and probe the impacts of interfacial electron loss on the PCE to approach the theoretical limit. The results led to a better understanding of the intrinsic mechanisms associated with the high PCE of the single TiO_2 nanowire QDHSC.

A nanoscale QDHSC was constructed from a single TiO_2 nanowire with uniformly coated CdSe QDs and connected to metallic Cu and Pt electrodes. The two electrodes have different work functions, which enabled the directional movement of charge carriers in the solar cell (Fig. 1a). The structure of the nanosized solar cell is mesoporous, similar to that of QD-based solar cells (Supplementary Fig. 1a); the band configurations are schematically depicted in Supplementary Fig. 1b. The charge-extraction strategies are similar to the heterojunction QD photovoltaics described by Sargent and co-workers[25]. When the light-emitting diode (LED) is switched on, as illustrated in Fig. 1b, the QDHSC is exposed to white light from the LED. Figure 1c presents a panoramic TEM image that shows the configuration of a QDHSC, which includes a TiO_2 nanowire, CdSe QDs and the contact electrodes. As evidenced by the TEM observation, the entire surface of the TiO_2 nanowire is covered with CdSe QDs. The HRTEM image of the QD-coated TiO_2 nanowire with the corresponding fast Fourier transformation pattern are shown in Fig. 1d. From the latter, a lattice fringe spacing of 0.35 nm was measured, which corresponds to the (101) plane of anatase TiO_2 (JCPDS no. 84-1286). The lattice spacing of the QD is around 0.26 nm, which can be assigned to the (102) planes of hexagonal CdSe (JCPDS no. 77-2307). We thus demonstrated that to install a LED light source in the TEM stage has no influence on the atomic-scale imaging capability of the TEM system (Supplementary Fig. 4 and Supplementary Part 4). This makes it possible to directly observe structure evolution in real time at the atomic level as well as to elucidate the photon–electron conversion processes that take place during the operation of the solar cell.

Representative current intensity–voltage (*J*–*V*) curves of the solar cells under light irradiation from the LED are shown in Fig. 1e. From Supplementary Fig. 7, the projected area of the TiO_2 nanowire under irradiation, which is the sum of the product of the nanowire length and diameter ($\sum d_i l_i$), can be estimated as ~4.8×10^4 nm^2 (the focus value for good HRTEM imaging was utilized to evaluate the horizontal states of the nanowires to ensure that nanowires stood perfectly horizontal under LED illumination during the electrical measurements (Supplementary Fig. 8)). This projected area

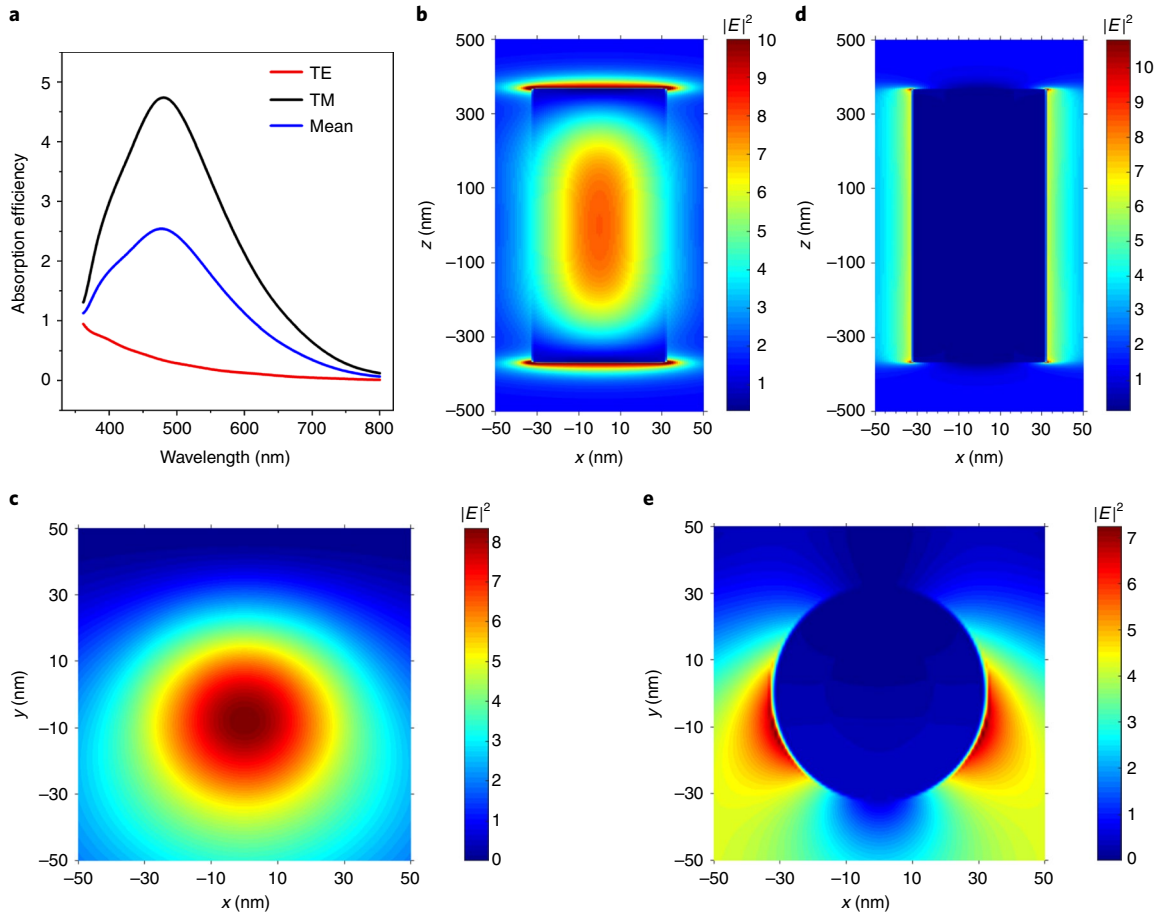

Fig. 2 | Enhanced absorption efficiency of a TiO_2-nanowire QDHSC. a, Light absorption efficiency for TE, TM and mean modes as a function of wavelength. **b**–**e**, Calculated electric field distribution ($|E|^2$, normalized to the incidence) of these structures for resonance that corresponds to the absorption peak at ~479 nm for the TM mode (**b**,**c**) and the TE mode (**d**,**e**).

was used to calculate the photocurrent density generated from the solar cells[26,27] (Supplementary Fig. 7). Based on the J–V curves (Fig. 1 e), the short circuit current density (J_{SC}), the open-circuit voltage (V_{OC}) and the fill factor were found to be 4.2 mA cm^{-2}, 0.38 V and 0.5, respectively. The solar cell, therefore, has an apparent PCE of 27.9 ± 2.4%. Repeating the experiment several times (Supplementary Fig. 9) confirmed that the measured photocurrent resulted only from the nanosized photovoltaic device. As a control experiment, the photocurrent was also measured on a bare TiO_2 nanowire without QDs decorated on the surface. Neither a photocurrent nor a photovoltaic effect was detected (Supplementary Fig. 10). It can therefore be concluded that the nanoscale QDHSC with simplified interfaces is able to utilize solar energy in a more efficient way than traditional QD-based solar cells.

Based on the J_{SC} and the incident power density, we can derive that the maximum external quantum efficiency can reach up to 140%, more than unity. To understand the origin of the unusually large J_{SC} and more than unity external quantum efficiency, we carried out finite-difference time-domain simulations on the QDHSC (Supplementary Part 5 and Supplementary Fig. 11). The optical absorption efficiency (Q_{abs}) under transverse electric (TE) or transverse magnetic (TM) illumination can be obtained by solving Maxwell's equations using a finite-difference time-domain method[28] (Supplementary Part 5). For the unpolarized light we used the mean Q_{abs} expressed as $(Q_{abs}^{TE} + Q_{abs}^{TM})/2$. Figure 2a shows the calculated wavelength dependence of Q_{abs} for TM, TE and the mean mode. There is an obvious resonance absorption near the wavelength of 479 nm, which matches well with our LED spectra peak location (Supplementary Fig. 12). The mean Q_{abs} at this resonance absorption is calculated to be 2.5, and mainly originates from the TM mode rather than the TE mode. To reveal the mechanism of resonance absorption, we plot the near-field distribution in the case of the resonance absorption peak for the TM mode in Fig. 2b,c. The near-field distribution for the TM mode has a maximum peak that corresponds to a ten times enhancement of the electric field intensity compared to the original incident one. The coupling here is so strong that the electric field can penetrate into the nanowire (Fig. 2b,c). For comparison, we also simulated the near-field distribution for the TE mode (Fig. 2d,e). The electric field intensity inside the nanowire was very low (around 0.1 of the incident light intensity) near the wavelength of 479 nm, as the electric field was usually confined outside the nanowire surface. Therefore, the electric field distribution demonstrates that the nanowire can, at specific wavelengths, absorb incident photons beyond its physical cross-section. This phenomenon is generally called the 'optical antenna effect'[29] and leads to the greatly enhanced resonance absorption and unusually large J_{SC}.

Carrier recombination at the defect sites, interfaces and surfaces is detrimental to the performance of solar energy conversion systems. Thus, the understanding and control of defects at the interface is crucial to improve the performance of solar cells. To elucidate the effect of interfaces and defects on the photovoltaic performance of the QDHSC, a direct in situ control over the interface area (S) during the photocurrent measurement is needed. This was achieved by

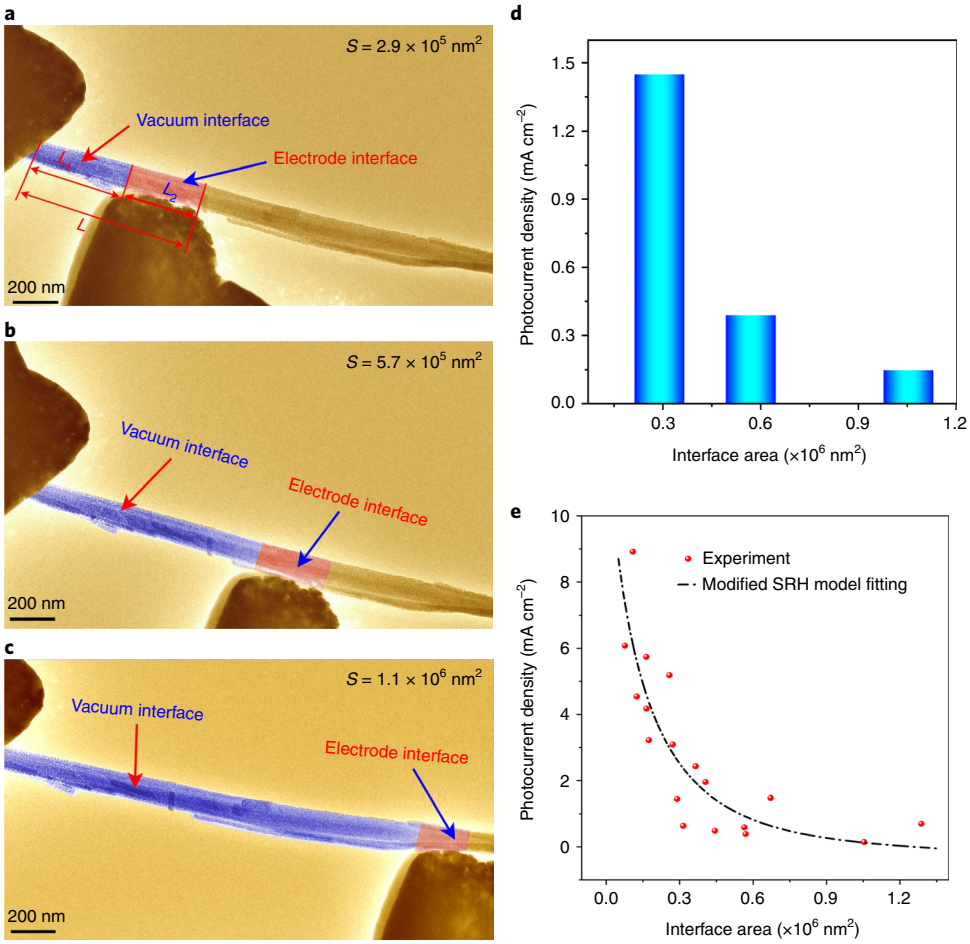

Fig. 3 | The dependence of the photocurrent on the interface area. a–c, Typical TEM images of QDHSC devices with the different interface areas (the interface is highlighted using false colour). **d**, Histogram of the photocurrent density from the recorded values in **a**, **b** and **c** as a function of their corresponding interface areas. **e**, Statistical distribution of the photocurrent density as a function of the interface area as compared to model fitted values. The data are fitted to the modified Shockley–Read–Hall (SRH) model; more details are given in Supplementary Part 6.

selecting the nanowire length (L) by precisely controlling the movement of the Pt tip (Fig. 3). The interfaces that serve as possible trap centres for charge recombination comprise (1) the exposed interface of the nanowire in vacuum, (2) the contact interface between the nanowire and Pt electrode and (3) the interface between the individual QDs and the nanowire. The total interface area S can be expressed by equation (1):

$$\begin{aligned} S &= S_{\text{vacuum}} + S_{\text{electrode}} + S_{\text{QD/NW}} \\ &= \left(\sum^{L_1} \pi L_i d_i + \sum^{L_2} L_i d_i\right) + \sum^{L_2} L_i d_i + 2\pi r^2 N \end{aligned} \quad (1)$$

where d is the diameter of the nanowire, L_1 is the shortest distance between the two electrodes (blue in Fig. 3 a–c), L_2 is the effective length after contact with the Pt electrode (red in Fig. 3c–e), r is the average radius of the QD and N is the number of QDs coated on the surface. The relationship between S and L is summarized in Supplementary Fig. 13. Integrating the measured experimental data presents the QDHSC as fabricated in the TEM, where each interface is indicated by a different colour (Fig. 3a–c). The QD loading density per square nanometre σ is estimated to be 0.0172 nm^{-2} and N is obtained from the relation $2\sigma dL$ (Supplementary Fig. 14). Thus the interface areas for the different measured lengths of the solar cells were calculated to be ~2.9×10^5, 5.7×10^5 and 1.1×10^6 nm^2, respectively (using equation (1)). In parallel, the change in photocurrent was recorded for solar cells with different nanowire lengths (Supplementary Fig. 15), which in turn correspond to different interface areas. The typical maximum photocurrent values obtained for solar cells with different interface areas are plotted in Fig. 3d. A decrease in photocurrent from 1.4 mA cm^{-2} down to 0.1 mA cm^{-2} was observed when the interface area increased from ~2.9×10^5 to 1.1×10^6 nm^2. To confirm this trend, we systematically examined a series of QDHSCs by changing the point of contact of the Pt tip with the TiO_2 nanowire and measured the photocurrent (as demonstrated in Supplementary Figs. 16–22).

Figure 3e presents the photocurrent density data collected on a QDHSC with different interface areas. In order to confirm optical antenna effect, we calculated Q_{abs} together with different interface area and wavelength, as shown in Supplementary Fig. 20. We found that TM mode contributes to enhancement beyond unity at the range of LED spectra and normalized Q_{abs} with LED spectra exhibits a decreasing trend with interface area. Notably, the measured photocurrents show a clear decreasing trend with increase in interface area of the solar cells; the data can be fitted using a modified Shockley–Read–Hall recombination model[30] on the premise that the total trap density N_T and the electron concentration are proportional to the interface area, and the carrier life time is inversely proportional to N_T (more details are given in Supplementary Part 6). In general, a larger interface area means a higher loading of QDs (combining the data from Fig. 3 and Supplementary Figs. 16–22, we see that the number

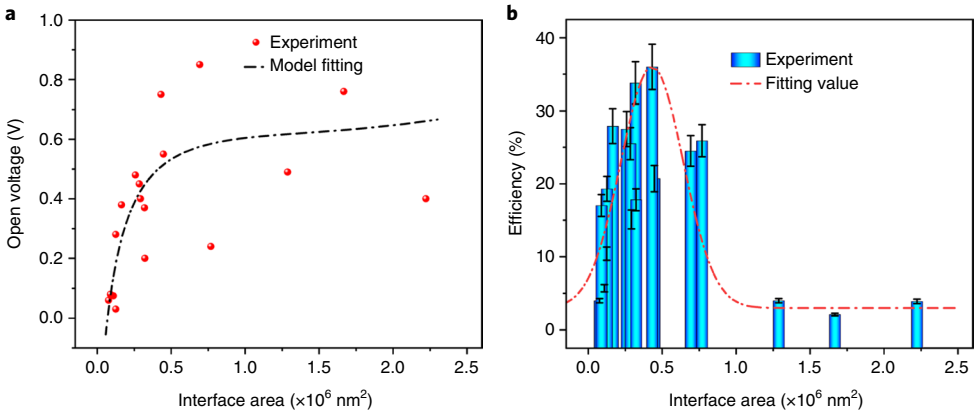

Fig. 4 | The effect of interface area on the open voltage and the efficiency of a single nanowire QDHSC. a, V_{OC} as a function of interface area along with results from data fitted to the model. **b**, Statistical distribution of the PCE as a function of the interface area of the QDHSC. The error bars are the efficiency error with the difference of light intensity irradiating on the sample induced by the geometry of the LED emission.

of QDs linearly increases with interface area, which in turn generates a greater number of photoelectrons (Supplementary Figs. 23 and 24). The photocurrent densities measured for the solar cells with larger interface areas, however, show an inverse trend, and are much lower than those collected on solar cells with a shorter nanowire. This decrease can be explained on the basis of the fitting model: a larger interface area leads to a larger number of defects, which increases the number of photoelectrons trapped at the defects. For longer nanowires, the carriers undergo a much longer collection time and thus suffer a great possibility being lost during the transport process. This lowers the photocurrent density, even though the larger interface area contributes to a larger number of electrons.

Apart from photocurrent density, the V_{OC} also determines the final conversion efficiency of solar cells. The change in open voltage of the QDHSC with interface area (Supplementary Figs. 25–30) is summarized in Fig. 4a. We fitted the experimentally obtained open voltage values as a function of S using the relationship between the photocurrent density and interface area in Fig. 3e, assuming that voltage reduction occurs mainly in the internal circuit[31]. From the results of the fitting, it is seen that the V_{OC} first shows a sharp increase with S below the value of $3\times10^5\,nm^2$ and levels off with further increase in S. The fitted equation can be expressed as[31,32]:

$$V = V_0 - V_1 = V_0 - \frac{kT}{q}\ln\left[1 + \frac{J}{A^* T^2 \exp(-q\phi_b/kT)}\right] \quad (2)$$

where V_0 is the intrinsic potential difference, V_1 is the voltage loss at the interface, k is the Boltzmann constant, T is the absolute temperature, q is the electronic charge, A^* is the Richardson constant, φ_b is the Schottky barrier height and J is the current density. The increase in V_{OC} is mainly attributed to the decreased V_1, that is, directly related to the decreased current density with increasing interface area[31,32]. Figure 4b is the statistical distribution of the PCE as a function of the interface area determined from the experimental data in Supplementary Figs. 25–30. The results from this statistical analysis can serve as a guideline to determine the optimal parameters that maximize the efficiency of the corresponding solar cells. Based on the data in Fig. 4b, we studied 11 devices with an optimized interface area of 1.3×10^5~$7.7\times10^5\,nm^2$ with consistent characteristics and an average PCE of $24.9\pm6.4\%$.

The low conversion efficiency of the mesoporous solar cell is usually attributed to the large number of defects and interfaces, which include (1) numerous grain boundaries, (2) interfaces in the semiconductor and (3) connecting necks in the nanoparticle film and electrodes. Therefore, photogenerated electrons may be easily trapped to recombine with holes, given that the electron transport in a nanoparticle film undergoes a multistep trapping and detrapping process (Fig. 5a)[33]. According to the diffusion equation, only free (untrapped) electrons in the conduction band can diffuse efficiently to the electrodes and contribute to the photocurrent density. To quantitatively assess the number of trapped electrons and free electrons, we calculated the values of n_c, the free electron density in the conduction band, and n_t, the electron density in trap states based on the model proposed by van de Lagemaat and Frank for mesoporous solar cells (Supplementary Part 7 gives more details)[34]. We found that n_t is nearly 10^6 times larger than n_c (Supplementary Fig. 31), which indicates that most of the photogenerated electrons in mesoporous solar cells are trapped by the high density of defects, which inhibits the effective charge injection and transport and results in a greatly lower PCE[35].

To further understand the effect of defect density on the photovoltaic performance and obtain a quantitative estimate, we set up a 1D diffusion equation to simulate the photovoltaic performance in a single nanowire solar cell, under the premise that the recombination of a photogenerated electron is proportional to the defect density in the solar cell (the derivation of this equation is given in Supplementary Part 8). In the mesoporous structure of conventional QDSCs, the interfaces (between TiO_2 particles) retard electron diffusion, as schematically illustrated in Fig. 5a. However, in the case of a single nanowire solar cell, this type of interface can be ignored, which means that the only existing interface is that associated with photoelectron injection and extraction. Therefore, the total density of defects N_T (cm^{-3}) in an optimized device in this work, estimated to be ~$10^9\,cm^{-3}$, was used in the simulation. This value of N_T is ~10^3 times lower than the value of ~$10^{12}\,cm^{-3}$ observed for mesoporous solar cells, estimated based on previous experimental results[30] (Fig. 5a,b). Under this assumption, the experimentally obtained photovoltaic characteristics agree with the results from calculation, as shown in Fig. 5c. This demonstrates that the ultrahigh efficiency of the QDHSC benefits from a simple structure and dramatically reduced defect density, and this design was realized by optimizing the interface using results from theoretical simulation. To compare the efficiency with that of mesoporous QD solar cell, we normalized the weighted integrated absorption of our LED spectra for the AM1.5 according to the factor G (ref. [36]) (Supplementary Part 9 discusses the rationality of using G):

$$G = \frac{\int P_{AM1.5}(\lambda)Q_{abs}(\lambda)d\lambda}{\int P_{LED}(\lambda)Q_{abs}(\lambda)d\lambda} \quad (3)$$

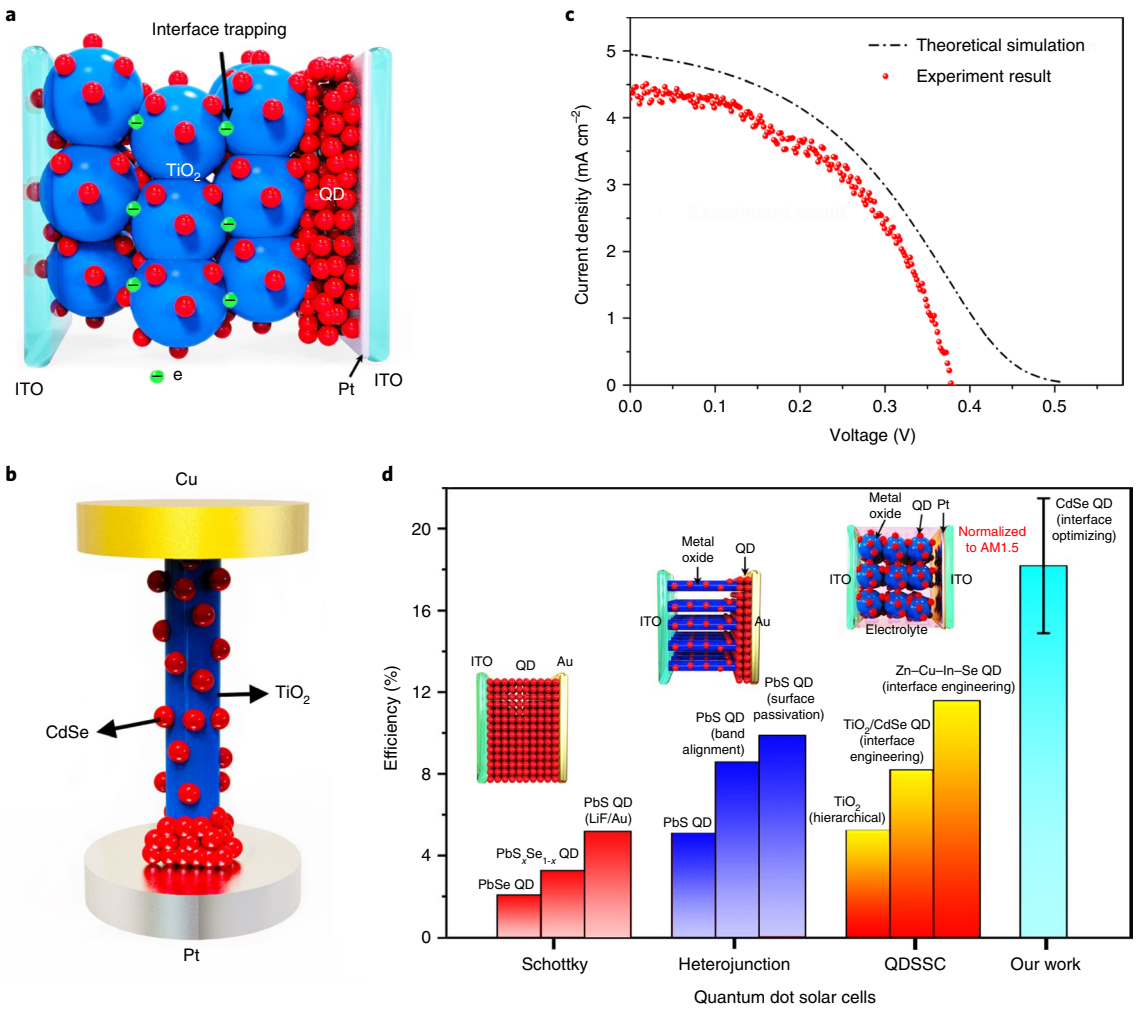

Fig. 5 | The mechanism of high efficiency and comparison of single nanowire QDHSCs. a, A schematic illustration of electron transport in a nanoparticle film shows different trapping processes. The photogenerated electrons may be easily trapped to recombine with holes due to the presence of a large number of traps at the surfaces and interfaces. **b**, A schematic diagram of our nanostructured QDHSC. The photogenerated electrons can be collected while minimizing losses from interface trapping. **c**, The current density versus voltage curves show experimental results along with the simulated photocurrent density–voltage curve (based on our new proposed model) while minimizing the concentration of trap states. The corresponding photovoltaic performance observed in our in situ experiment is also shown, which is in accordance with the results from theoretical predictions, and is much larger than the results based on the macroscopic model. **d**, Comparison of the efficiency obtained in our study versus those of the QDSCs reported in the literature. QDSSC, quantum dot sensitized solar cell; ITO, indium tin oxide.

where $P_{AM1.5}$ and P_{LED} are normalized unity light intensities. We calculated that G is 1.4 according to the LED spectra and AM1.5. Figure 5d compares the reported conversion efficiencies of conventional QDHSCs of different types with that, normalized to AM1.5, of the QDHSC designed in this work. The single nanowire QDHSC reported here delivers an efficiency of $17.8 \pm 4.5\%$, which is almost 1.5 times higher than the certified efficiency recorded to date. A previous work reported that an improvement of up to 5–10% was achieved by employing a heterojunction structure to enable a more efficient charge collection as compared to the initial efficiency of 2–5% obtained using a Schottky junction. More recently, an efficiency of 11.6% was obtained by exploiting new material QDs and the interface engineering of QD by coating it with an inorganic compound to reduce recombination at the interface[7]. By optimizing the interfaces, we show that efficiency can be further improved significantly. Our study could thus offer important guidelines to the design of high-performance quantum-dot-based solar cells, and could inspire new improved structures with optimized interfaces to approach the theoretical efficiency limit.

We have developed an effective strategy for the in situ construction of a single nanowire QD solar cell inside a TEM, which allowed precise tuning of the interface in the nanoscale heterojunction solar cells to achieve a nearly ideal quantum efficiency. Our results highlight the critical role of interfacial defects on the photocarrier generation and extraction, and offer valuable insight on the design of high-efficiency solar cells with a minimum defect density and an optimized charge collection efficiency. An optical antenna effect may also be exploited to further boost the photocurrent of the nanoscale solar cell devices (Supplementary Fig. 32). The methodologies developed here can also be extended to the design and investigation of other types of solar cells and optoelectronic devices.

Online content

Any methods, additional references, Nature Research reporting summaries, source data, statements of code and data availability and associated accession codes are available at https://doi.org/10.1038/s41565-019-0526-7.

Received: 21 August 2018; Accepted: 16 July 2019;
Published online: 26 August 2019

References

1. Kamat, P. V. Quantum dot solar cells. Semiconductor nanocrystals as light harvesters. *J. Phys. Chem. C* **112**, 18737–18753 (2008).
2. Tian, J. et al. Constructing ZnO nanorod array photoelectrodes for highly efficient quantum dot sensitized solar cells. *J. Mater. Chem. A* **1**, 6770–6775 (2013).
3. Sambur, J. B., Novet, T. & Parkinson, B. A. Multiple exciton collection in a sensitized photovoltaic system. *Science* **330**, 63–66 (2010).
4. Semonin, O. E. et al. Peak external photocurrent quantum efficiency exceeding 100% via MEG in a quantum dot solar cell. *Science* **334**, 1530–1533 (2011).
5. Hanna, M. C. & Nozik, A. J. Solar conversion efficiency of photovoltaic and photoelectrolysis cells with carrier multiplication absorbers. *J. Appl. Phys.* **100**, 074510 (2006).
6. Shockley, W. & Queisser, H. J. Detailed balance limit of efficiency of p–n junction solar cells. *J. Appl. Phys.* **32**, 510–519 (1961).
7. Du, J. et al. Zn–Cu–In–Se quantum dot solar cells with a certified power conversion efficiency of 11.6%. *J. Am. Chem. Soc.* **138**, 4201–4209 (2016).
8. Shen, Q., Kobayashi, J., Diguna, L. J. & Toyoda, T. Effect of ZnS coating on the photovoltaic properties of CdSe quantum dot-sensitized solar cells. *J. Appl. Phys.* **103**, 084304 (2008).
9. Fan, S.-Q. et al. Highly efficient CdSe quantum-dot-sensitized TiO_2 photoelectrodes for solar cell applications. *Electrochem. Commun.* **11**, 1337–1339 (2009).
10. Lee, Y.-L. & Lo, Y.-S. Highly efficient quantum-dot-sensitized solar cell based on co-sensitization of CdS/CdSe. *Adv. Funct. Mater.* **19**, 604–609 (2009).
11. Lee, H. et al. Efficient CdSe quantum dot-sensitized solar cells prepared by an improved successive ionic layer adsorption and reaction process. *Nano Lett.* **9**, 4221–4227 (2009).
12. Li, L. et al. Highly efficient CdS quantum dot-sensitized solar cells based on a modified polysulfide electrolyte. *J. Am. Chem. Soc.* **133**, 8458–8460 (2011).
13. Jin-nouchi, Y., Naya, S. I. & Tada, H. Quantum-dot-sensitized solar cell using a photoanode prepared by in situ photodeposition of CdS on nanocrystalline TiO_2 films. *J. Phys. Chem. C* **114**, 16837–16842 (2010).
14. Sun, Z. et al. Continually adjustable oriented 1D TiO_2 nanostructure arrays with controlled growth of morphology and their application in dye-sensitized solar cells. *CrystEngComm* **14**, 5472–5478 (2012).
15. Sun, Z., Kim, J. H., Zhao, Y., Attard, D. & Dou, S. X. Morphology-controllable 1D–3D nanostructured TiO_2 bilayer photoanodes for dye-sensitized solar cells. *Chem. Commun.* **49**, 966–968 (2013).
16. Chen, X. Y., Ling, T. & Du, X. W. Low-temperature synthesis of ZnO/CdS hierarchical nanostructure for photovoltaic application. *Nanoscale* **4**, 5602–5607 (2012).
17. Sudhagar, P. et al. High open circuit voltage quantum dot sensitized solar cells manufactured with ZnO nanowire arrays and Si/ZnO branched hierarchical structures. *J. Phys. Chem. Lett.* **2**, 1984–1990 (2011).
18. Zhu, Z., Qiu, J., Yan, K. & Yang, S. Building high-efficiency CdS/CdSe-sensitized solar cells with a hierarchically branched double-layer architecture. *ACS Appl. Mater. Interfaces* **5**, 4000–4005 (2013).
19. Zhao, K. et al. Boosting power conversion efficiencies of quantum-dot-sensitized solar cells beyond 8% by recombination control. *J. Am. Chem. Soc.* **137**, 5602–5609 (2015).
20. Huang, J. Y. et al. In situ observation of the electrochemical lithiation of a single SnO_2 nanowire electrode. *Science* **330**, 1515–1520 (2010).
21. Xu, F. et al. Visualization of lithium-ion transport and phase evolution within and between manganese oxide nanorods. *Nat. Commun.* **8**, 15400 (2017).
22. Liu, Q. et al. Real-time observation on dynamic growth/dissolution of conductive filaments in oxide-electrolyte-based ReRAM. *Adv. Mater.* **24**, 1844–1849 (2012).
23. Miller, B. K. & Crozier, P. A. System for in situ UV–visible illumination of environmental transmission electron microscopy samples. *Microsc. Microanal.* **19**, 461–469 (2013).
24. Cavalca, F. et al. Light-induced reduction of cuprous oxide in an environmental transmission electron microscope. *Chem. Cat. Chem.* **5**, 2667–2672 (2013).
25. Lan, X., Masala, S. & Sargent, E. H. Charge-extraction strategies for colloidal quantum dot photovoltaics. *Nat. Mater.* **13**, 233 (2014).
26. Tian, B. et al. Coaxial silicon nanowires as solar cells and nanoelectronic power sources. *Nature* **449**, 885–889 (2007).
27. Tang, J., Huo, Z., Brittman, S., Gao, H. & Yang, P. Solution-processed core–shell nanowires for efficient photovoltaic cells. *Nat. Nanotechnol.* **6**, 568–572 (2011).
28. Cao, G. et al. Design of μc-Si:H/a-Si:H coaxial tandem single-nanowire solar cells considering photocurrent matching. *Opt. Express* **22**, A1761–A1767 (2014).
29. Kempa, T. J., Day, R. W., Kim, S.-K., Park, H.-G. & Lieber, C. M. Semiconductor nanowires: a platform for exploring limits and concepts for nano-enabled solar cells. *Energ. Environ. Sci.* **6**, 719–733 (2013).
30. Nepal, J., Sadegh Mottaghian, S., Biesecker, M. & Farrokh Baroughi, M. Modeling of trap assisted interfacial charge transfer in dye sensitized solar cells. *Appl. Phys. Lett.* **102**, 203503 (2013).
31. Zhang, S., Yang, X., Numata, Y. & Han, L. Highly efficient dye-sensitized solar cells: progress and future challenges. *Energ. Environ. Sci.* **6**, 1443–1464 (2013).
32. Ni, M., Leung, M. K. H., Leung, D. Y. C. & Sumathy, K. Theoretical modeling of TiO_2/TCO interfacial effect on dye-sensitized solar cell performance. *Sol. Energy Mater. Sol. Cells* **90**, 2000–2009 (2006).
33. De Jongh, P. E. & Vanmaekelbergh, D. Trap-limited electronic transport in assemblies of nanometer-size TiO_2 particles. *Phys. Rev. Lett.* **77**, 3427–3430 (1996).
34. Van de Lagemaat, J. & Frank, A. J. Effect of the surface-state distribution on electron transport in dye-sensitized TiO_2 solar cells: nonlinear electron-transport kinetics. *J. Phys. Chem. B* **104**, 4292–4294 (2000).
35. Tian, J. & Cao, G. Control of nanostructures and interfaces of metal oxide semiconductors for quantum dots sensitized solar cells. *J. Phys. Chem. Lett.* **6**, 1859–1869 (2015).
36. Abass, A., Shen, H., Bienstman, P. & Maes, B. Angle insensitive enhancement of organic solar cells using metallic gratings. *J. Appl. Phys.* **109**, 023111 (2011).

Acknowledgements

This research was supported by National Key Research and Development Program of China (2017YFA0204800), the Natural National Science Foundation of China (Grant nos. 11327901, 11525415, 51420105003, 61106055, 11774051, 61574034 and 61601116), the National Basic Research Program of China (2015CB352106), the Fundamental Research Funds for the Central Universities (2242018K41020). Z.S. appreciates the financial support from the Australian Research Council (ARC) through an ARC Future Fellowship project (FT180100387) and a Discovery Project (DP160102627).

Author contributions

H.D., F.X., Z.Z. and L.S. conceived and designed the experiments. H.D. performed the experiments. H.D., Z.S., L.S., Z.Z. and X.D. analysed the data and constructed the paper. Y.Z. performed the finite-difference time-domain simulation. L.S. contributed materials and analysis tools. H.D. and Z.S. co-wrote the paper with all the authors contributing to the discussion and preparation of the manuscript.

Competing interests

The authors declare no competing interests.

Additional information

Supplementary information is available for this paper at https://doi.org/10.1038/s41565-019-0526-7.

Reprints and permissions information is available at www.nature.com/reprints.

Correspondence and requests for materials should be addressed to Z.Z., X.D. or L.S.

Peer review information: *Nature Nanotechnology* thanks Giorgio Divitini and the other, anonymous, reviewer(s) for their contribution to the peer review of this work.

Publisher's note: Springer Nature remains neutral with regard to jurisdictional claims in published maps and institutional affiliations.

Methods

Sample preparation. TiO_2 nanowires were purchased from Plasma Chem GmbH. Mercaptopropionic acid-capped CdSe QDs in aqueous solution were prepared using previously reported procedures[37]. The nanowires were immersed in a solution of QDs for 2 h and then rinsed sequentially with water and ethanol. The result TiO_2 nanowire/CdSe QDs were centrifuged and dried for further in situ TEM experiments.

Assembly of a single nanowire QDHSC inside a TEM for the in situ experiment. In our in situ experiment, the CdSe QD-coated TiO_2 nanowire was mounted on a copper electrode by immersing a copper grid into the TiO_2 nanowire/CdSe QD solution in ethanol. The movable metallic electrode was a platinum tip, which was controlled by a piezo-tube to make contact with the CdSe QD-coated TiO_2 nanowire mounted on the copper grid. We used Ga–In liquid metal with a liquidus temperature of 15 °C to mount the Pt tip, as shown in Supplementary Fig. 33. This can be used to effectively reduce the contact resistance though the formation of a liquid/solid interface after the contact with the nanowire. The QDHSC designed in the present work has a similar band configuration to typical QD-based solar cells, except that we used a copper electrode instead of an ITO electrode, which has a similar work function, ~4.7 eV. The resultant potential difference between the two electrodes is expected to guide the movement of the photogenerated carriers. Electrons were injected from the CdSe to TiO_2 and then to Cu, and holes transported from the CdSe to Pt. To mount the single nanowire QDHSC on the holder, a copper grid loaded with the sample, which contained individual TiO_2 nanowires coated with CdSe QDs, was placed on the fixed sapphire substrate below to face a light source, which here was a LED acting as a solar light simulator.

To confirm no oxidized copper formed, which would presumably shift the energy levels significantly, in our experiment the copper grid was cut in half beforehand and one-half immediately placed into the TEM. An EDX analysis on this Cu grid confirmed that no oxidation of the copper occurred via this treatment, as shown in Supplementary Fig. 34. The photoelectric properties of the individual nanowire QDHSC were measured inside a TEM (Titan 80–300, FEI) using a custom-made nanofactory in situ STM-TEM electrical probe, which was modified to be equipped with a white LED (power intensity of 2.74~3.26 mW cm^{-2} (Supplementary Fig. 35 gives details)) to function as a light source. To solve the LED light-induced drift that potentially changes in the contact, we designed a stable d.c. output voltage system to power the LED illumination instead of commercial batteries (Supplementary Part 4). This was also used to reduce thermal drift during the LED operation, which could change the geometry and might not be observed if the TEM beam was blanked. The drift with LED light irradiation after stabilization presented almost no change compared with the drift of the nanowire under dark conditions. The drift speed in the light condition was almost the same as that in dark condition, and thus thermal drift during the LED operation at the nanoscale did not result in a change in geometry at the nanoscale. The Pt counter electrode was driven by a piezoelectric tip to contact the fixed TiO_2 nanowires stepwise, with a minimum step distance of 20 pm. Finally, the Pt electrode was attached to the QD-coated TiO_2 nanowire on the Cu electrode to form a nanoscale QDHSC. A Keithley 6430 source meter with a subpicoamp resolution was used to measure the photoelectric performance of the solar cell, including current–voltage and current–time curves (Supplementary Fig. 36 gives the current measurement methods). The combination of the shield system and the subpicoamp galvanometer enables the in situ photoelectric TEM stage to measure the photocurrent with a resolution of 0.2 pA (Supplementary Part 3 and Supplementary Fig. 3e).

Data availability

The data that support the plots within this paper and other findings of this study are available from the corresponding author upon reasonable request.

References

37. Pan, Z. et al. Near infrared absorption of $CdSe_xTe_{1-x}$ alloyed quantum dot sensitized solar cells with more than 6% efficiency and high stability. *ACS Nano* **7**, 5215–5222 (2013).